

Microstructures with extraordinary dynamic work hardening and strain rate sensitivity in $\text{Al}_{0.3}\text{CoCrFeNi}$ high entropy alloy

Sindhura Gangireddy^a, Bharat Gwalani^a, Kaimiao Liu^b, Rajarshi Banerjee^a, Rajiv S. Mishra^a

^aAdvanced Materials and Manufacturing Processes Institute, University of North Texas, Denton, TX 76207

^bMaterials Science and Engineering, University of North Texas, Denton, TX 76207

Abstract:

$\text{Al}_{0.3}\text{CoCrFeNi}$ is an FCC-based high entropy alloy (HEA) that can display a wide spectrum of mechanical properties. Cold work and precipitation are good strengthening mechanisms in this HEA, and their effect on dynamic work hardening and strain rate sensitivity (SRS) was investigated. Dynamic deformation testing using split-Hopkinson pressure bar (SHPB) at $2 \times 10^3 \text{ s}^{-1}$ and quasistatic tensile deformation at 10^{-3} s^{-1} were conducted on thermomechanically processed conditions. The HEA behaved like a conventional FCC alloy with higher flow stresses and work hardening in the dynamic regime. All the conditions showed substantial dynamic work hardening due to the low stacking fault energy (SFE) of the HEA. Precipitates enhanced twinning, as observed from post-SHPB deformed microstructures, and resulted in an extraordinary work hardening rate $> 2200 \text{ MPa}$. Cold work introduced large-scale deformation twins and these suppressed further twin nucleation during testing, and a lower work hardening of 1000 MPa was observed. SRS was highly microstructure-sensitive and varied from an exceptional $m = 0.063$ in the cast condition, where the biggest flow stress contributor is solute strengthening of short-range nature and can be thermally activated. Introduction of long-range athermal incoherent precipitates reduced SRS slightly. Cold work, which introduces much higher density of athermal defects, dislocations and large-scale deformation twins, drastically reduced SRS to $m = 0.006$. Upon annealing the rolled material, partial recovery of cold work and precipitation occurred together and coupled to result in a moderate SRS, $m = 0.02$.

Keywords: Dynamic mechanical behavior, work hardening, strain rate sensitivity, FCC-based high entropy alloy, $\text{Al}_{0.3}\text{CoCrFeNi}$.

Introduction:

High-entropy alloys (HEAs) are a new paradigm of metallic alloy development of stabilizing simple microstructures with multiple principal elements in equimolar proportions. Significant multi-element effects as compared with conventional alloys were proposed in HEAs; e.g., high entropy, sluggish diffusion, lattice distortion, and cocktail effects and have been studied extensively [1-4]. These remarkable mechanical strength, resistance to corrosion, and creep properties of alloy systems have fascinated many researchers in last decade. Investigations of chemical and structural stability of these alloys and the unique structure-property relationship are alone intriguing. The mechanical properties, in particular, are of crucial importance in engineering. $\text{Al}_x\text{CoCrFeNi}$ is prominent among the several alloy systems identified on the basis of simple crystal structure design strategy; it changes from FCC to BCC structure with increasing aluminum content, and displays a wide range of mechanical behavior [5-8]. $\text{Al}_{0.3}\text{CoCrFeNi}$ ($x=0.3$) is an FCC-based alloy with low Al content, which is single phase in the cast condition, but precipitates intermetallic phases upon high-temperature annealing. Previous studies have confirmed that Hall-Petch and precipitation strengthening mechanisms can be used to significantly enhance mechanical properties [9]. The stacking fault energy (SFE) of similar FCC-based HEAs, CrFeCoNi and CrMnFeCoNi, is reported to lie between 20 - 30 mJ/m² [10]. With addition of Al in CrFeCoNi, the SFE is expected to decrease further [11], and hence, $\text{Al}_{0.3}\text{CrFeCoNi}$ is estimated to have a very low SFE. So,

unlike the conventional *FCC* metals which do not generally twin until appreciable plastic strain [12], these HEAs have a higher propensity for twinning leading to strong strain hardening. The strength gains from cold working can hence be substantial. Moreover, with the high concentration of solute atoms, the multi-element HEAs offer potential for enhanced strain rate sensitivity (SRS). However, SRS is a microstructurally-sensitive parameter [13] and can vary significantly as the microstructure is modified by these different strengthening mechanisms. In this study, we generated vastly diverse microstructures by thermomechanically processing $\text{Al}_{0.3}\text{CoCrFeNi}$ HEA in two routes: one to induce pure precipitation, and another with both precipitation and cold work strengthening. A combined study of their dynamic mechanical response from split-Hopkinson pressure bar (SHPB) testing in the strain rate regime of $2 \times 10^3 \text{ s}^{-1}$, as well as standard tensile testing results at quasi-static strain rate of 10^{-3} s^{-1} , was conducted to understand the microstructural dependence of SRS. Microstructural investigations explored processed conditions and deformation mechanisms.

Experimental Procedure:

A combination of cold work and precipitation strengthening mechanisms were studied by subjecting the *FCC*-based high entropy alloy (HEA) $\text{Al}_{0.3}\text{CoCrFeNi}$ to two categories of processing conditions: (a) cold roll + solutionizing + annealing, (b) cold roll followed directly by annealing (Figure 1). The composition of the cast ingot obtained from EDAX analysis is presented in Table 1. This cast material was initially homogenized briefly at high temperatures to eliminate any elemental segregation and to bring it to single-phase *FCC* before cold-rolling. In the first processing route, this strained material was first subjected to a solutionizing step of high temperature and long duration of 1 hour to cause full recrystallization and growth of *FCC* grains. All the conditions that underwent this route would therefore have similar grain sizes. The subsequent annealing step determined the nature, size, and distribution of the precipitate formation. In the second route of directly annealing the cold-worked material, the pre-strained grains sometimes simultaneously underwent partial recrystallization along with precipitation. The nature and number density of the precipitates formed changed significantly in the cold-worked, strained, and defect-rich grains compared to the recrystallized grains even though annealing treatments remained the same. The microstructures are discussed in detail in the results section.

Table 1. Elemental composition of the cast ingot.

	Wt (%)	At (%)
Al	3.38	6.81
Cr	22.28	23.31
Fe	22.98	22.38
Co	25.65	23.67
Ni	25.71	23.82
Total	100	100

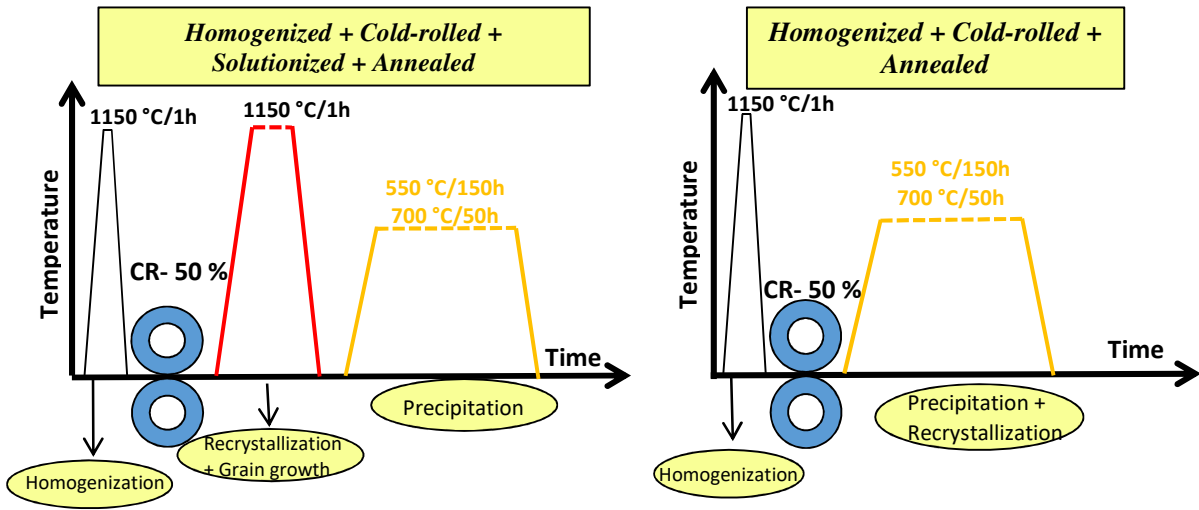


Figure 1. Processing routes of (Left) indirect, and (Right) direct annealing treatments.

Results and Discussion:

Microstructures

The microstructures resulting from indirect annealing are shown in Figure 2. The solutionized alloy, 50% cold-roll + 1150°C/1h, (CRSA) was single-phase FCC with grains of ~150 µm. The selected area diffraction pattern (SADP) from [110] FCC zone axis (ZA) showed only the fundamental FCC reflections. Subsequent annealing at 550°C/150h (CRSA-550) formed nanoscale L₁₂ precipitates. This sample exhibited additional super lattice reflections at {001} and {011} positions in the [110] FCC diffraction pattern (inset). The corresponding dark field (DF) image recorded from the super-lattice spot marked with a circle in the SADP pattern clearly revealed the ordered L₁₂ precipitates of spherical form, with size ranging from 3 to 10 nm. The other indirect annealed condition of 700°C/50h (CRSA-700) formed coarser B₂ precipitates. This sample exhibited grain boundary precipitation and some intragranular precipitation of coarse second-phase precipitates exhibiting a lath-like morphology. SADP recorded from a grain boundary precipitate could be consistently indexed as the [110] BCC ZA. Additionally, {001} superlattice reflections in this BCC diffraction pattern indicated that the grain boundary precipitates are B₂ (ordered BCC). A bright field of a near grain boundary region showed the FCC matrix did not have L₁₂ ordering at this temperature.

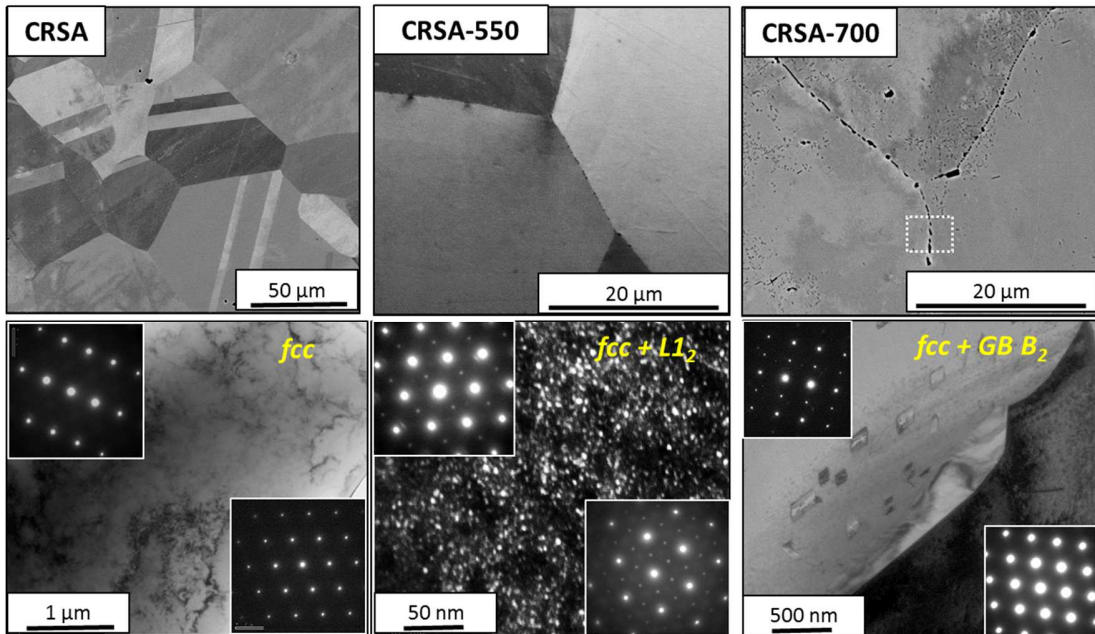


Figure 2. Microstructures from the indirect annealing route: (Left) solutionized (CRSA), (Middle) 50% Cold-roll + 1150°C/1h + 550°C/150h (CRSA-550), and (Right) 50% Cold-roll + 1150°C/1h + 700°C/50h (CRSA-700) conditions. (Top) SEM images, and (Below) TEM images with SADP diffraction patterns confirming the precipitate phases present.

Microstructures from the second route of directly annealing the cold-rolled material are depicted in Figure 3. At 550°C/150h (CR-550), direct annealing resulted in partial recrystallization besides precipitation, forming a complex microstructure composed of some recrystallized fine grains along with the coarse strained FCC prior-grains, as well as globular B₂ and σ precipitates at the grain boundaries. Therefore the precipitates ended up occurring more predominantly in the fine grained recrystallized regions with larger concentrations of grain boundaries. Direct annealing at 700°C/50h (CR-700), on the other hand, did not show any recrystallization but formed a higher concentration of B₂ precipitates than indirect annealing. Even as the B₂ morphology after both CRSA-700 and CR-700 treatments was similar, being lath-like and elongated, it was more homogeneously distributed in CR-700 instead of populating only the grain boundary as in CRSA-700. CR-700 also had large globular σ precipitates at the grain boundaries. Thermodynamic predictions at these temperatures in this alloy using CALPHAD approach [14,15] suggest only FCC + B₂ phase as major phases. The σ phase is expected in the Al_xCoCrFeNi HEA system at only high Al contents, $x > 0.9$ [16,17]. However, the rolled material with pre-strained grains with several lattice defect sites and higher energy appeared to overcome the high interfacial energy barrier for formation of σ and B₂ precipitates with a different crystal structures in an FCC matrix. So, while these precipitates can have extremely sluggish kinetics to reach thermodynamic equilibrium in a defect-free recrystallized structure, both σ and B₂ precipitation could occur more abundantly during annealing of the deformed structure. Key observations included a change in the experimentally observed phase composition at 550°C, increased concentration of B₂ at 700°C, and occurrence of σ phase in both conditions. A competition between recrystallization and precipitation was also observed at 550°C and 700°C. At 550°C, recrystallization occurred concurrently with B₂ and σ precipitation; whereas at 700°C, B₂ and σ precipitation superseded recrystallization and reduced excess free energy, thereby suppressing the driving force for recrystallization.

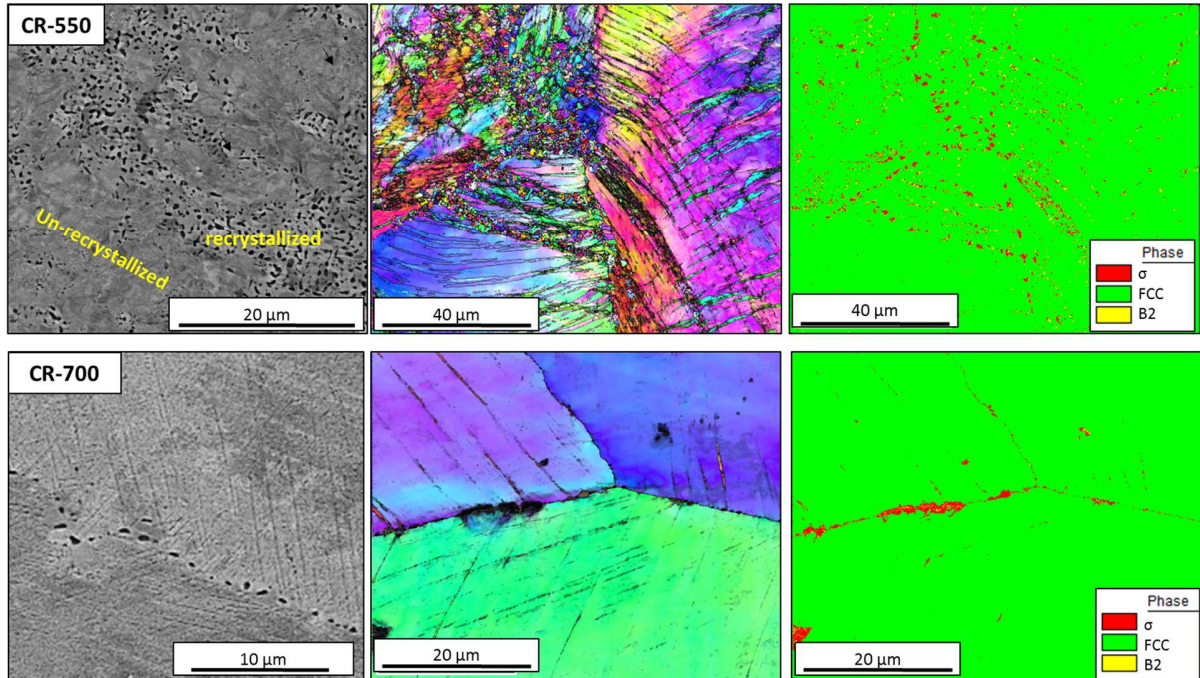


Figure 3. Microstructures from the direct annealing route: (Top) 50% Cold-roll + 550°C/150h (CR-550), and (Bottom) 50% Cold-roll + 700°C/50h (CR-700) conditions. (Left) SEM, (Middle) EBSD, and (right) phase maps showing the σ , B₂, and FCC distribution.

Mechanical Response:

The five different microstructural conditions from the above two processing routes were subjected to quasi-static tensile testing at 10^{-3} s^{-1} strain rate as well as dynamic compression testing at $2 \times 10^3 \text{ s}^{-1}$ strain rate using split-Hopkinson pressure bar (SHPB) technique. They showed a wide range of strength and ductility combinations in the quasi-static regime (Figure 4(a)). The solutionized single phase FCC material showed very low strength with YS of only 115 MPa, but a high ductility of over 64%. On the other end of this spectrum was the directly annealed 550°C/150h material with a high YS of 812 MPa but with very low ductility of 5%. The other conditions showed strength-ductility combinations that fall in between these two extremes. The stress-strain curves in the high strain rate regime (10^3 s^{-1}) are depicted in Figure 4(b). The dynamic response also followed a similar trend as the quasi-static data with respect to the microstructural conditions. But due to higher strain rate, all conditions showed both higher stresses as well as higher work hardening. This behavior is typical of FCC alloys where higher stresses arise from the thermal activation component of solute strengthening [18,19]. In conventional high-SFE alloys, dynamic recovery at high strain rates is suppressed due to insufficient time for reorganization and annihilation of accumulated dislocations, resulting in higher work hardening. In Al_{0.3}CoCrFeNi HEA where the stacking fault energy is very low [11], the the partials would be sufficiently dissociated to [20] inhibit cross-slip even at low strain rates. As the twin boundary energy is proportional to SFE for most metals [21], low SFE also promotes deformation twinning. With continual introduction of new interfaces, twinning enhances work hardening in a dynamic Hall-Petch effect reducing the mean free path of dislocations [20]. So low SFE of this alloy is attributed to be the cause for the considerable work hardening even in the quasi-static regime observed in our data. At high strain rates, there would be a combination of

further suppression of dynamic recovery due to reduced time for dislocation mobility, and enhanced twinning activity from higher stresses including secondary twins and twin-twin interactions. Slip and twinning were discovered to be parallel processes in another low SFE FCC HEA CoCrFeMnNi, as reported by Moon et al. [22] at 77K in 10^{-3} s $^{-1}$ - 10^{-2} s $^{-1}$ strain rate range, conditions akin to dynamic regime at RT. With continual introduction of new interfaces, twinning enhances work hardening [20] in dynamic conditions.

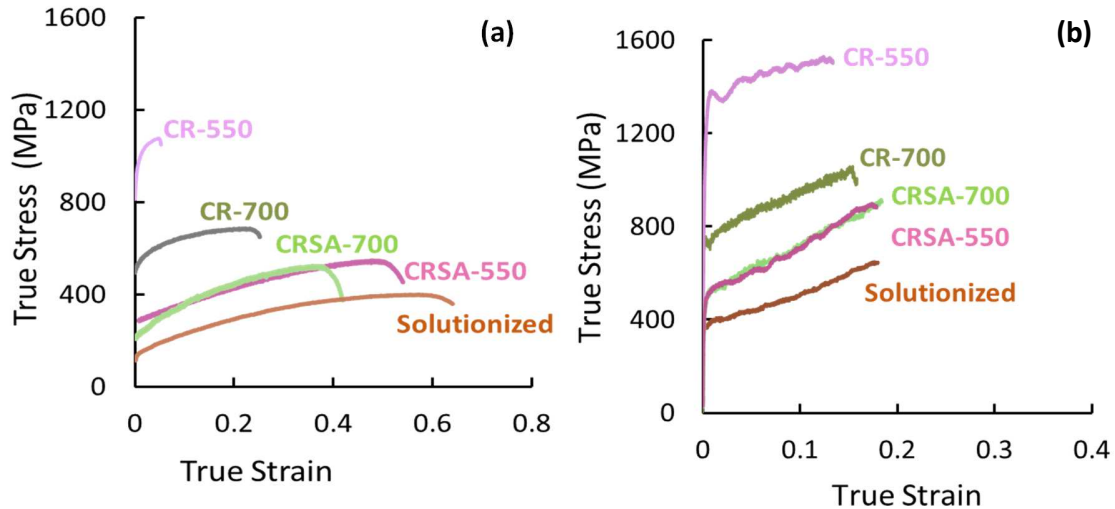


Figure 4. Comparison of the stress-strain curves of the different microstructures produced by direct and indirect annealing of 50% cold worked $\text{Al}_{0.3}\text{CoCrFeNi}$ alloy: (a) Quasi-static testing at 10^{-3} s $^{-1}$ (b) dynamic testing using SHPB at a strain rate of 2×10^3 s $^{-1}$.

The effect of precipitation can be deciphered clearly by comparing the solutionized material with the indirectly annealed materials; i.e., CRSA vs. CRSA-550/CRSA-700. These three microstructures had similar grain sizes. It is evident that the presence of precipitates, either in the form of uniformly distributed nano-sized L1₂ precipitates (CRSA-550) or larger lath-like B₂ precipitates at grain boundaries (CRSA-700), resulted in moderate strengthening with higher YS, UTS, and HSR flow stresses. Ductility was lowered but not excessively. Precipitates act as barriers to dislocation motion, and their back stresses make them potential twin nucleation sites, enhancing overall twinning activity, a phenomenon often observed in aged HCP metals [23]. Figure 5(a) compares microstructures of indirectly annealed CRSA-550 condition prior- and post-SHPB testing. Before the test, the microstructure had defect-free recrystallized grains with some annealing twins; but after the test, extensive twinning was observed. Misorientation profiling (in the insets) along the highlighted lines confirmed the dark lines in the EBSD images to be twin fault planes with their characteristic 60° misorientation. The other annealed condition, CRSA-700, also exhibited heavy twinning. Both CRSA-550 and CRSA-700 demonstrated astounding dynamic work hardening rates $d\sigma/d\epsilon = 2453$ MPa and 2217 MPa, respectively. On the other hand, the microstructure of directly annealed CR-700 condition after SHPB testing indicated very limited twinning activity, and showed a much more moderate $d\sigma/d\epsilon = 1255$ MPa. Enhanced deformation twinning was therefore associated with this spike in the dynamic work hardening rate.

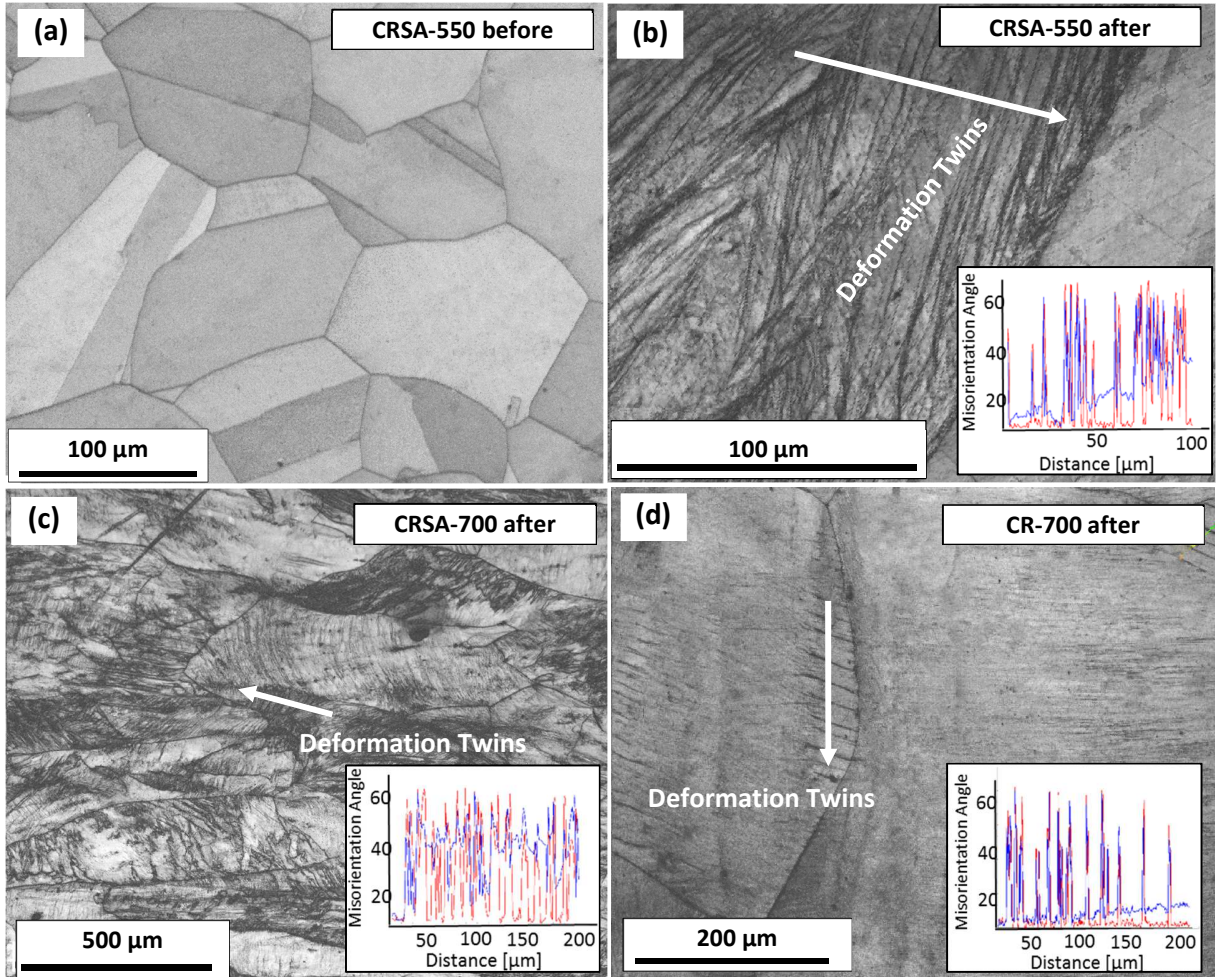


Figure 5. EBSD images comparing the deformation twinning in post-SHPB microstructures of indirectly and directly annealed conditions: (a) CRSA-550 before testing, (b) CRSA-550 after dynamic deformation showing extensive twinning, (c) CRSA-700 after dynamic deformation also showing heavy twinning, and (d) CR-700 after dynamic deformation showing limited twinning activity.

In the second route of direct annealing, the effects of σ + B_2 precipitation and cold work were combined. In order to understand cold-work strengthening independently, the mechanical properties of pure-rolled material (50%CR) from both strain rate regimes were obtained and are compared to the solutionized material in Figure 6. Pure cold work was a much stronger strengthening mechanism than precipitation, originating from low SFE of this HEA. Figure 6(a) shows 50% thickness reduction increased the yield strength upto ~ 800 MPa. However, the drop in ductility was also very sharp, and the material failed at < 15% strain. Upon direct annealing this cold worked material at 700°C/50h (CR-700), ductility was improved with an associated loss in strength, which indicated partial recovery of the cold work. At 550°C/150h (CR-550), however, strength was much higher than even the pure-rolled material, and was attributed to a high density of σ phase, which provides pronounced hardening [24]. This embrittling phase also severely reduced ductility to 5% in CR-550. In the CR-700, the σ phase was much less prevalent, as it occurred only at grain boundaries, which are scarce in this coarse-grained microstructure. In CR-550, σ precipitates were far more pervasive, occurring at the multitude of

boundaries in the fine grained recrystallized regions. Due to the high Hall-Petch constant of this HEA, estimated to be ~ 824 MPa/ $\mu\text{m}^{0.5}$ [9], grain size reduction from 150 μm to a couple of μm in the recrystallized region would result in an increase of this region's strength from 115 MPa to 515 MPa. Thus grain boundary strengthening in these recrystallization regions would also be a strong contributor in CR-550.

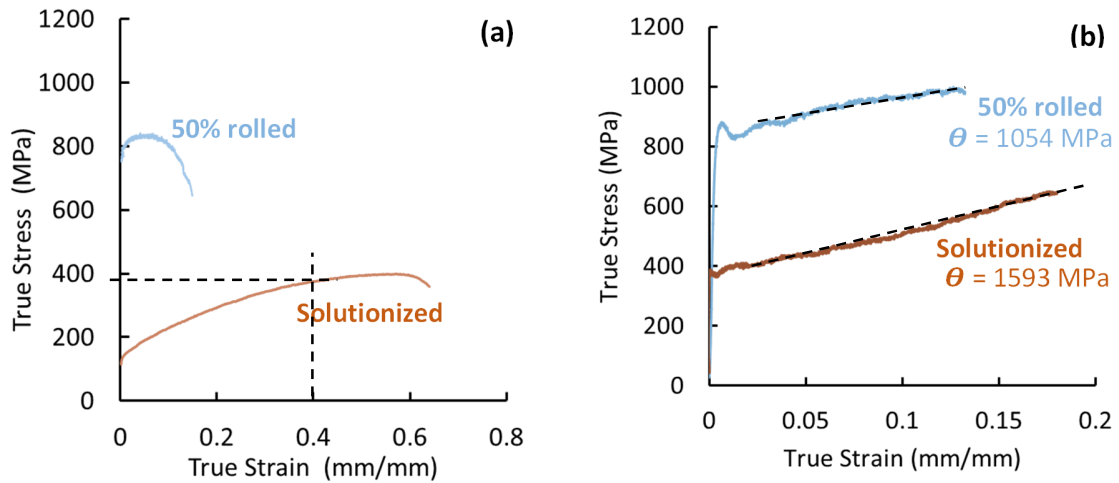


Figure 6. Comparison of the (a) quasi-static (10^3 s^{-1}), and (b) dynamic stress-strain curves ($2 \times 10^3 \text{ s}^{-1}$) of 50% cold worked and solutionized conditions.

The cold worked material also depicted an obvious reduction in the dynamic work hardening rate (Figure 6(b)). After rolling, the microstructure showed evidence of a high density of deformation twinning. Figure 7 displays its EBSD map along with misorientation profiling of two highlighted lines. The 60° misorientation of the features crossed over by these misorientation profiles confirmed that they were twin fault planes. Such a presence of large prior-twins would suppress new twin formation during SHPB deformation, while a large initial dislocation density would promote dynamic recovery. The coupled effect resulted in lowering of dynamic work hardening from 1593 MPa of the solutionized condition to 1054 MPa in the 50% CR condition.

While the YS of the rolled material was ~ 800 MPa after 50% thickness reduction (equivalent to a uniaxial true strain of 0.4), the quasi-static stress-strain curve of the solutionized condition reaches only 390 MPa at this strain level. On the other hand, the dynamic stress-strain curve with a slope of 1600 MPa gives flow stresses of ~ 1000 MPa at 0.4 strain. This incongruity in the strain path is attributed to deformation twinning activity, which is clearly strain rate dependent. Rolling mill is actually a sub-dynamic deformation process and the deformation rate would lie in between the two strain rate regimes. Figure 7 shows an EBSD map of the rolled microstructure which shows clear evidence of twin-twin interactions between large deformation twins, and smaller secondary twins intersecting them. Mishra et al [25] have proposed a framework for plastic deformation based on implications of lattice strain on dislocations and twins. In addition to CrFeCoNi system creates a very large atomic misfit of Al atoms (7% in $\text{Al}_{0.3}\text{CoCrFeNi}$) and thus an overall enormous lattice distortion. It is suggested that the energy for dislocation nucleation is likely to be lower in such HEAs along with twin energy values, but the solutes dampen dislocation motion, and so encouraging mechanical twinning. Therefore these complex concentrated alloys usually display a low SFE [11] that is accompanied by a low twin boundary

energy [21-Meyers2001]. Twinning is a strain rate dependent phenomenon. Dynamic deformation at high strain rates where time is insufficient for dislocation recovery leads to enhanced twinning activity [26]. So the extent of mechanical twinning at any given strain would be higher in the sub-dynamic process of rolling mill than the quasi-static tensile test procedure. Twins reduce the mean free path of dislocations and cause hardening. The higher YS of 800 MPa in the rolled microstructure, compared to the quasi-static curve prediction of 390 MPa, must therefore arise from the extensive deformation twinning observed in Figure 7.

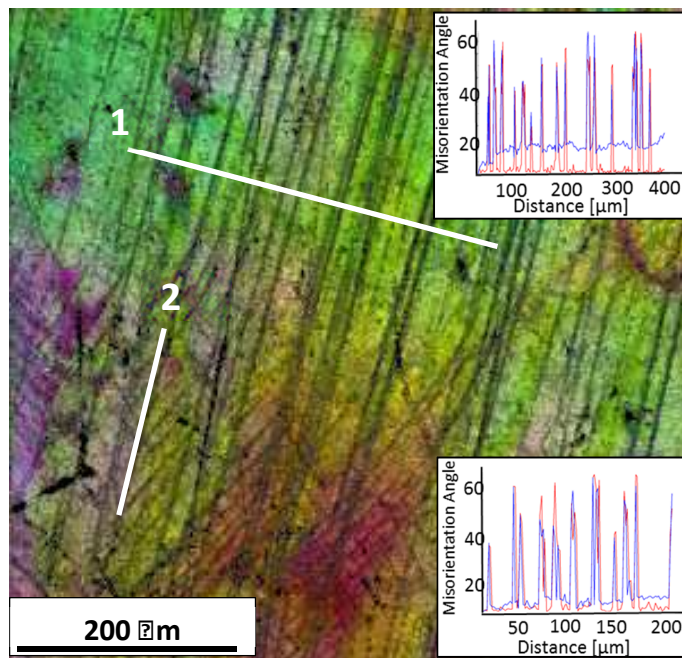


Figure 7. EBSD map, with Inverse Pole Figure overlaid with Image Quality, of 50% cold-rolled material. (Insets) Misorientation profiling along the two highlighted lines showing the 60° misorientation of twin fault planes.

Strain Rate Sensitivity (SRS):

One fascinating observation from Figure 6 is that even as the pure-rolled material had a high YS of ~ 800 MPa at LSR, dynamic flow stress was only around 850 MPa. CRSA-550 in Figure 6, on the other hand, showed dynamic flow stresses reaching over 1400 MPa, while having a comparable YS. This contrasting behavior indicated that strain rate sensitivities (SRS) of these two conditions were very different. Therefore the effect of strain rate on each of the conditions was examined (Figure 8).

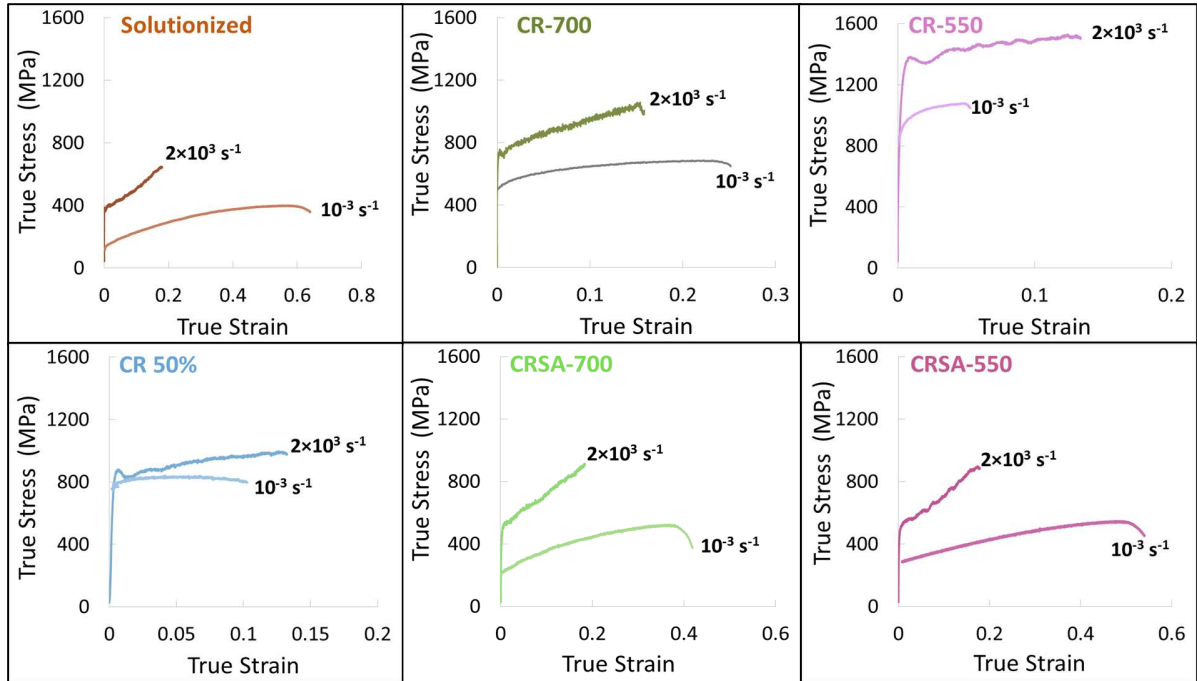


Figure 8. Comparison of the quasi-static and dynamic stress-strain curves of the 50% cold-rolled, solutionized, direct annealed, and indirect annealed conditions.

Except for the pure-rolled material, all other conditions showed significant surge in the flow stresses with an increase of strain rate by six orders of magnitude, from 10^{-3} s^{-1} to $2 \times 10^3 \text{ s}^{-1}$. The strain rate sensitivity parameter, m , calculated from flow stresses for each of the above six microstructures is summarized in Table 2.

$$m = \left[\frac{\partial \ln \sigma}{\partial \ln \dot{\varepsilon}} \right]_{T=RT, \varepsilon=0.01} \quad (1)$$

Table 2. Summary of strain rate sensitivity (SRS) of the microstructures of 50% cold-worked, direct and indirect annealed $\text{Al}_{0.3}\text{CoCrFeNi}$ alloy conditions.

	Strain rate sensitivity, m
CRSA (50CR+1150°C/1h)	0.063
CRSA-700 (50CR+1150°C/1h +700°C/50h)	0.054
CRSA-550 (50CR+ 1150°C/1h +550°C/150h)	0.044
CR-700 (50CR+700°C/50h)	0.022
CR-550 (50CR+550°C/150h)	0.017
Pure-rolled (50CR)	0.006

Obviously, SRS varied significantly across these six conditions, depending on the nature of obstacles introduced into the original microstructure by thermomechanical processing. SRS originates from thermal activation [18], and SRS dependence of microstructure can be understood through a classification of obstacles to the dislocation motion in a given microstructure. Long-range obstacles such as grain boundaries (σ_{GB}), twin boundaries (σ_{TW}), dislocations on other planes (σ_{DIS}), and incoherent precipitates (σ_{PPT}) are athermal and have no dependence on strain rate/temperature. On the other

hand, thermal activation can help overcome short-range barriers such as solutes (σ_{SS}) and Pierls-Nabarro/ friction stress (σ_{FS}). Strain rate dependence of a condition will depend on the relative contributions from these components to total stress [27].

$$\sigma = (\underbrace{\sigma_{FS} + \sigma_{SS}}_{\text{(Thermal)}}) + (\underbrace{\sigma_{GB} + \sigma_{DIS} + \sigma_{TW} + \sigma_{PPT}}_{\text{(Athermal)}}) \quad (2)$$

In typical FCC metals, internal stresses (the first two thermal terms in the above equation) are considered insignificant. But for HEAs, large friction stress values were reported due to significant lattice distortion and varying dislocation mobility [28]. HEAs are also reported to have large P-N barriers as Wu et al observed from severe temperature dependence of tensile properties of CoCrFeMnNi HEA [29]. With multiple solute atoms, the HEAs also demonstrated strong solid solution strengthening [30]. A small SFE also causes the dislocations to split into wide partials [20], and their cross-slip needs more thermal activation. Hence the low SFE of the HEA [11] also contributes further to SRS. So in the solutionized material, a simple microstructure with relatively defect-free coarse single phased FCC grains, the main obstacles are short-range, except for the few grain boundaries.

$$\sigma_{CRSA} = (\underbrace{\sigma_{FS} + \sigma_{SS}}_{\text{(Thermal)}}) + (\underbrace{\sigma_{GB}}_{\text{(Athermal)}}) \quad (3)$$

Grain boundary strengthening can be estimated from the Hall-Petch constant in literature, 824 MPa/ $\mu\text{m}^{0.5}$ [9], and the grain size of the solutionized condition, 150 μm , as $\sigma_{GB} = 67$ MPa. Therefore, the internal stresses must be contributing the remainder of the total strength of this condition $\sigma_{CRSA} = 157$ MPa. So the thermal contributions, $\sigma_{FS} + \sigma_{SS} = 90$ MPa, were comprised of a large fraction of the total strength, and this condition demonstrated a high SRS with $m = 0.063$. Li et al [31] also reported high SRS of 0.053 in a coarse grained microstructure of single-phase FCC Al_{0.3}CoCrFeNi.

In the indirectly annealed conditions, the microstructure was very akin to the solutionized condition but for the presence of precipitates. Athermal stresses from precipitates are expected to lower SRS, but not significantly, because their overall contribution to strength remained mild (Figure 4(a)). In CRSA-700, the lath-like B₂ precipitates were located along the grain boundaries. These incoherent precipitates and the grain boundaries are both long range, athermal barriers and are overlapped location wise. So this lowered SRS only slightly, $m = 0.054$. In CRSA-550, the L1₂ precipitates were homogeneously distributed throughout the grain interior and SRS lowered a little further to $m = 0.044$.

$$\sigma_{CRSA-700/550} = (\underbrace{\sigma_{FS} + \sigma_{SS}}_{\text{(Thermal)}}) + (\underbrace{\sigma_{GB} + \sigma_{PPT}}_{\text{(Athermal)}}) \quad (4)$$

On the contrary, cold-rolling introduced a high density of lattice defects, dislocations and deformation twins, which were long-range and athermal obstacles (Figure 7). These now became greater contributors to strength, as was evident from the significant rise in YS to 780 MPa upon cold work (Figure 6(a)). As only a minor fraction of strength is derived from internal stresses, the pure-rolled material had very weak SRS, with an order of magnitude lower m of 0.006.

$$\sigma_{50\%CR} = (\underbrace{\sigma_{FS} + \sigma_{SS}}_{\text{(Thermal)}}) + (\underbrace{\sigma_{GB} + \sigma_{DIS} + \sigma_{TW}}_{\text{(Athermal)}}) \quad (5)$$

Annealing this rolled material directly, long durations and high treatment temperatures would significantly reduce cold work in the grains. However, the direct annealed conditions also had σ phase at grain boundaries. In CR-700, the greater concentrations of lath-like B_2 were homogeneously distributed throughout the grains; while CR-550 had partial recrystallization and these fine grains had a higher prevalence of grain boundary B_2 along with σ precipitates. These incoherent precipitates would also make athermal contributions. In CR-550, the effect of partial recrystallization forming defect-free small grains is offset by the increased density of grain boundaries. Compared to the solutionized condition, the complex microstructure of CR-550 had three kinds of additional athermal contributions:

$$\sigma_{CR-550} - \sigma_{CRSA} = X \beta \left[\frac{1}{\sqrt{d}} - \frac{1}{\sqrt{D}} \right] + (1 - X) (\sigma_{50\%CR,remnant}) + \sigma_{PPT} \quad (6)$$

where X is the fraction of recrystallized regions, d is the recrystallized grain size, D is the original grain size, β is the Hall-Petch constant, and $\sigma_{50\%CR,remnant}$ is the remnant cold work in the form of dislocation or twin density retained in the prior grains even after annealing. Therefore, obstacles of both nature were present in the direct annealed conditions: thermally activated short-range ones such as Peierls-Nabarro and solute atoms; and athermal long-range ones such as incoherent precipitates, remnant cold work, and formation of new grain boundaries. Hence, a moderate strain rate dependence in between the two extremes of solutionized and pure-rolled conditions with $m \sim 0.02$ was observed.

Equation 1 of SRS derivation from two stress-strain curves acquired at different strain rates originates in the strain rate dependent plastic deformation in viscoplastic behavior given as:

$$\sigma = K \dot{\varepsilon}^m \quad (7)$$

where K is a constant and σ is the total flow stress given by a summation of strain-rate dependent thermal stress ($\sigma_t(\dot{\varepsilon})$), and strain rate independent athermal stress (σ_a).

$$\sigma = \sigma_t(\dot{\varepsilon}) + \sigma_a \quad (8)$$

Let us consider an extreme situation with an extremely coarse material where grain size $\rightarrow \infty$, resulting in the athermal stresses $\sigma_a \rightarrow 0$. Let the SRS of this condition be m_0 , which represents a limiting value for the maximum SRS that can be attained in this material.

$$\sigma_t(\dot{\varepsilon}) = K \dot{\varepsilon}^{m_0} \quad (9)$$

Derivative of Equation 8 by strain rate $\dot{\varepsilon}$,

$$\frac{d\sigma}{d\dot{\varepsilon}} = \frac{d\sigma_t(\dot{\varepsilon})}{d\dot{\varepsilon}} + \frac{d\sigma_a}{d\dot{\varepsilon}} = Km \dot{\varepsilon}^{m-1}$$

As athermal stresses do not have strain rate dependence, $\frac{d\sigma_a}{d\dot{\varepsilon}} = 0$. Using Equation 9 to get a derivative of thermal stresses,

$$Km_0 \dot{\varepsilon}^{m_0-1} + 0 = Km \dot{\varepsilon}^{m-1}$$

$$\frac{\dot{\varepsilon}^{m_0}}{\dot{\varepsilon}^m} = \frac{m}{m_0} \quad (10)$$

So the relative contribution from thermal stresses to total strength can be written as:

$$\frac{\sigma_t(\dot{\varepsilon})}{\sigma_t(\dot{\varepsilon}) + \sigma_a} = \frac{K \dot{\varepsilon}^{m_0}}{K \dot{\varepsilon}^m} = \frac{\dot{\varepsilon}^{m_0}}{\dot{\varepsilon}^m}$$

From Equation 10,

$$\frac{\sigma_t(\dot{\varepsilon})}{\sigma_t(\dot{\varepsilon}) + \sigma_a} = \frac{m}{m_0} \quad (11)$$

So we can forecast that SRS, m , would increase linearly with relative contribution of thermal stress. For this material, the internal stresses are: $\sigma_t(\dot{\varepsilon}) = \sigma_{FS} + \sigma_{SS} = 90$ MPa, as calculated earlier. The experimentally calculated SRS values are compared to the ratio of thermal stress to total yield strength in each of these different conditions (Table 3). A limiting case where the thermal contributions approach zero $\sigma_t(\dot{\varepsilon}) \rightarrow 0$, resulting in the SRS also approaching zero $m \rightarrow 0$, is also included. Figure 9 plots SRS as a function of $\frac{\sigma_t(\dot{\varepsilon})}{\sigma_t(\dot{\varepsilon}) + \sigma_a}$, and shows a linear relationship as expected from Equation 11. The slope of this graph would be m_0 , the maximum SRS possible in this material, and is obtained as 0.123.

Table 3 Summary of thermal stress, yield stress, dynamic flow stress, relative contribution of internal stresses to total yield stress, and strain rate sensitivity of the different microstructural conditions.

	$\sigma_t(\dot{\varepsilon} = 10^{-3})$ (MPa)	$\sigma(\dot{\varepsilon} = 10^{-3})$ (MPa)	$\sigma(\dot{\varepsilon} = 2 \times 10^3)$ (MPa)	$\frac{\sigma_t(\dot{\varepsilon} = 10^{-3})}{\sigma(\dot{\varepsilon} = 10^{-3})}$	$m = \left[\frac{\partial \ln \sigma}{\partial \ln \dot{\varepsilon}} \right]$
CRSA	90	157	390	0.573	0.063
CRSA-700	90	233	525	0.386	0.054
CRSA-550	90	285	540	0.316	0.044
CR-700	90	543	757	0.166	0.022
CR-550	90	1037	1325	0.087	0.017
50%CR	90	801	875	0.112	0.006
Limit case				0	0

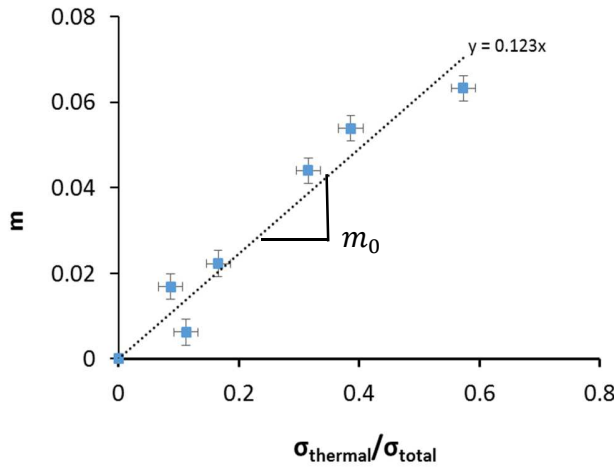


Figure 9. Variation of strain rate sensitivity with the relative thermal contributions to total yield stress in the different microstructural conditions. A linear relationship between m and $\frac{\sigma_t(\dot{\varepsilon})}{\sigma_t(\dot{\varepsilon}) + \sigma_a}$ is observed with a slope that is equivalent to the limiting SRS, $m_0 = 0.123$.

Conclusions:

Strength, ductility, work hardening, and strain rate sensitivity in $\text{Al}_{0.3}\text{CoCrFeNi}$ HEA alloy were highly sensitive to microstructure. Thermomechanical processing generated a variety of microstructures and mechanical properties. The two routes followed in this study were: cold-rolling followed by direct annealing vs. cold-rolling followed by solutionizing and subsequent annealing. The solutionized material, from the latter route, had a simple structure of single-phase *FCC*, coarse recrystallized grains of $\sim 150\ \mu\text{m}$. Subsequent annealing was useful in studying the effect of pure precipitation, forming L1_2 at low temperature (CRSA-550) and B_2 at high temperature (CRSA-700). The cold-rolled material was used to investigate the added influence of cold work and associated introduction of large deformation twins and dislocation density. The direct route yielded a combination of both strengthening mechanisms due to their complex microstructures of coarse, strained grains, with precipitates; and a small fraction of tiny recrystallized grains (CR-550) or partially recovered structures with higher density of precipitates (CR-700). The major takeaways from their mechanical behavior are summarized below:

- (a) **Strength-Ductility:** The low strength of the regular single phase grained structure was improved by precipitation annealing without any significant loss of ductility. Cold work was more effective in improving strength but simultaneously lowered ductility. A combination of cold work and high temperature annealing resulted in a good combination of strength-ductility.
- (b) **Work hardening:** Due to the low SFE, this HEA showed high work hardening in all conditions investigated. Precipitation greatly enhanced twinning and improved work hardening beyond 2200 MPa in the dynamic regime. Cold work had an opposite effect and reduced work hardening to 1000 MPa.
- (c) **Strain rate sensitivity (SRS):** An extraordinary range of strain rate sensitivities were observed, $m = 0.006\text{-}0.063$, with microstructural variation. Due to the plethora of intrinsic obstacles thermal contributions are significant in HEAs and lead to much superior SRS than conventional coarse grained *FCC* alloys. The solutionized single-phased coarse-grained structure showed $m = 0.063$. Precipitation caused a slight reduction owing to the athermal nature of the precipitate obstacles. Pure cold work yielded the lowest strain rate sensitivity of $m=0.006$ due to introduction of a large density of athermal obstacles, dislocation and deformation twins, which contribute significantly to strength. Subsequent annealing reduced defect density but with additional athermal contributions from incoherent precipitates, yielding a moderate $m \sim 0.02$. SRS varied linearly with the relative fraction of thermal stresses in total yield stress. The true SRS attained in a defect free condition, was derived to be 0.123, which represents the upper limit possible for this material.

Acknowledgment:

The work was performed under a cooperative agreement between the Army Research Laboratory and the University of North Texas (W911NF-16-2-0189). We also acknowledge the Materials Research Facility at the University of North Texas for microscopy facilities.

References:

1. Gao, M. C. "High-Entropy Alloys". Springer International Publishing, 2016.
2. Yeh, J.W. "Novel alloy concept, challenges and opportunities of high-entropy alloys." B. Raj (Ed.), *Frontiers Design Materials*, CRC Press (2007): 31-47.
3. Tsai, M-H. "High-entropy alloys: a critical review." *Materials Research Letters* 2.3 (2014): 107-123.

4. Zhang, Y. "Solid-solution phase formation rules for multi-component alloys." *Advanced Engineering Materials* 10.6 (2008): 534-538.
5. Wang, W.R. "Phases, microstructure and mechanical properties of $\text{Al}_x\text{CoCrFeNi}$ high-entropy alloys at elevated temperatures." *Journal of Alloys and Compounds* 589 (2014): 143-152.
6. Wang, W.R. Effects of Al addition on the microstructure and mechanical property of $\text{Al}_x\text{CoCrFeNi}$ high-entropy alloys. *Intermetallics* 26 (2012): 44-51.
7. Joseph, J. "Understanding the mechanical behaviour and the large strength/ductility differences between FCC and BCC $\text{Al}_x\text{CoCrFeNi}$ high entropy alloys." *Journal of Alloys and Compounds*, 726 (2017): 885-895.
8. Chou, H.P. "Microstructure, thermophysical and electrical properties in $\text{Al}_x\text{CoCrFeNi}$ ($0 \leq x \leq 2$) high-entropy alloys". *Materials Science and Engineering: B* 163.3 (2009): 184-189.
9. Gwalani, B. "Optimizing the coupled effects of Hall-Petch and precipitation strengthening in a $\text{Al}_{0.3}\text{CoCrFeNi}$ high entropy alloy." *Materials & Design* 121 (2017): 254-260.
10. Zaddach, A.J. "Mechanical properties and stacking fault energies of NiFeCrCoMn high-entropy alloy". *JOM* 65.12 (2013): 1780-1789.
11. Kumar, N. "High strain-rate compressive deformation behavior of the $\text{Al}_{0.1}\text{CrFeCoNi}$ high entropy alloy." *Materials & Design* 86 (2015): 598-602.
12. Zhang, D. Deformation twinning (update). Reference Module in Materials Science and Materials Engineering (doi: 10.1016/B978-0-12-803581-8.02878-2) (2016).
13. Gao, C. Y. "Constitutive modelling of plasticity of fcc metals under extremely high strain rates." *International Journal of Plasticity* 32 (2012): 121-133.
14. Gwalani, B. "Stability of ordered L12 and B2 precipitates in face centered cubic based high entropy alloys- $\text{Al}_{0.3}\text{CoFeCrNi}$ and $\text{Al}_{0.3}\text{CuFeCrNi}_{2.1}$." *Scripta Materialia* 123 (2016): 130-134.
15. Gwalani, B. "Cu assisted stabilization and nucleation of L1 2 precipitates in $\text{Al}_{0.3}\text{CuFeCrNi}_{2.1}$ fcc-based high entropy alloy." *Acta Materialia* 129 (2017): 170-182.
16. Wang, W.R. "Phases, microstructure and mechanical properties of $\text{Al}_x\text{CoCrFeNi}$ high-entropy alloys at elevated temperatures." *Journal of Alloys and Compounds* 589 (2014): 143-152.
17. Tsai, M.H. "Criterion for sigma phase formation in Cr-and V-containing high-entropy alloys." *Materials Research Letters* 1.4 (2013): 207-212.
18. Gray III, G.T. "High-strain-rate deformation: mechanical behavior and deformation substructures induced." *Annual Review of Materials Research* 42 (2012): 285-303.
19. Follansbee, P.S. "High-strain-rate deformation of FCC metals and alloys." *Metallurgical applications of shock-wave and high-strain-rate phenomena* 1.1 (1986): 451-479.
20. Otto, F. "The influences of temperature and microstructure on the tensile properties of a CoCrFeMnNi high-entropy alloy." *Acta Materialia* 61.15 (2013): 5743-5755.
21. Meyers, M. A. "The onset of twinning in metals: a constitutive description." *Acta materialia* 49.19 (2001): 4025-4039.
22. Moon, J. "On the strain rate-dependent deformation mechanism of CoCrFeMnNi high-entropy alloy at liquid nitrogen temperature." *Materials Research Letters* 5.7 (2017): 472-477.

23. Robson, J.D. "Effect of particles in promoting twin nucleation in a Mg–5 wt.% Zn alloy." *Scripta Materialia* 63.8 (2010): 823-826.
24. Tsai, M.H. "Significant hardening due to the formation of a sigma phase matrix in a high entropy alloy." *Intermetallics* 33 (2013): 81-86.
25. Mishra, R. S. "Lattice strain framework for plastic deformation in complex concentrated alloys including high entropy alloys." *Materials Science and Technology* 31.10 (2015): 1259-1263.
26. Li, Z. "Adiabatic shear localization in the CrMnFeCoNi high-entropy alloy." *Acta Materialia* 151 (2018): 424-431.
27. Follansbee, P.S. "A constitutive description of the deformation of copper based on the use of the mechanical threshold stress as an internal state variable." *Acta Metallurgica* 36.1 (1988): 81-93.
28. Kumar, N. "Friction stir processing of a high entropy alloy Al 0.1 CoCrFeNi." *JOM* 67.5 (2015): 1007-1013.
29. Wu, Z. "Temperature dependence of the mechanical properties of equiatomic solid solution alloys with face-centered cubic crystal structures." *Acta Materialia* 81 (2014): 428-441.
30. Zhang, Y. "Alloy design and properties optimization of high-entropy alloys." *JOM* 64.7 (2012): 830-838.
31. Li, Z. "High-velocity deformation of Al 0. 3 CoCrFeNi high-entropy alloy: Remarkable resistance to shear failure." *Scientific Reports* 7 (2017): 42742.